Supporting Information for: Inhomogeneous Surface Plasmon Polaritons

Jonathan J. Foley IV, Jeffrey M. McMahon, George C. Schatz, Hayk Harutyunyan, Gary P. Wiederrecht, Stephen K. Gray

Contents

List of Figures

1 Transmission and reflection coefficients

The main text focuses on the waveforms of the refracted SPPs or ISPPs by appropriately adapting Snell's law ideas to 2-D SPP propagation from one effective metal-dielectric medium into another effective metal-dielectric medium. In a similar fashion one can adapt Fresnel equations to this problem and infer both the reflection amplitude for SPPs to go back into the first medium and the transmission amplitude for the ISPP in the second medium. Paralleling the discussion by Chang and co-workers[1], we find the complex ISPP transmission coefficient,

$$t = \frac{2(\eta_1 \cos(\theta_1) + i\kappa_1 \cos(\theta_1))}{(\eta_1 \cos(\theta_1) + i\kappa_1 \cos(\theta_1)) + (N_2 \cos(\theta_2) + iK_2 \cos(\phi_2))}, \quad (1)$$

and the complex ISPP reflection coefficient,

$$r = \frac{(\eta_1 \cos(\theta_1) + i\kappa_1 \cos(\theta_1)) - (N_2 \cos(\theta_2) + iK_2 \cos(\phi_2))}{(\eta_1 \cos(\theta_1) + i\kappa_1 \cos(\theta_1)) + (N_2 \cos(\theta_2) + iK_2 \cos(\phi_2))}, \tag{2}$$

where we assume that the magnetic permeability is unity on either side of the interface. We note that for SPP refraction, the plane of incidence is parallel to the metal surface, so the appropriate reflection and transmission coefficients are for s-polarized waves. The transmission and reflection amplitudes have the form

$$T = |t|^2 \left(\frac{N_2 \cos(\theta_2) + iK_2 \cos(\phi_2)}{\eta_1 \cos(\theta_1) + i\kappa_1 \cos(\theta_1)} \right) \tag{3}$$

and

$$R = |r|^2. \tag{4}$$

The ISPP electric field intensity is proportional to the transmission amplitude multiplied by the electric field intensity of the incident SPP,

$$|\mathbf{E}_2|^2 = T\ |\mathbf{E_1}|^2. \tag{5}$$

The expression Eq. 5 gives the intensity at the interface; the ISPP loses amplitude along the direction given by ϕ_2.

2 ISPP propagation and confinement lengths

For brevity we will always refer to the complex generalization of Snell's law, Eqs. (5) and (6) of the text, as simply Snell's law. Figure S1 shows the Snell's law and FDTD electric field intensities for the example of an SPP excited on a gold surface, refracting at a gold/silver interface, and leading to an ISPP on the silver surface as discussed in the text. The Snell's law propagation length (L_P) and confinement length (L_C) can be computed from the formulae given in the text, and depend on the refraction angles θ_2 and ϕ_2 as well as the imaginary part of the effective medium index, K_2. To extract the same quantities from the FDTD results, we sample electric field intensities along the propagation direction and in the direction perpendicular to the propagation direction.Exponentials of the form $|\mathbf{E}_0|^2 \exp(-r/L_i)$ are fit to the sampled data to extract L_P and L_C, where r is the distance along the appropriate scan direction. Note Fig. S1 we sample approximately 5 μm along $\hat{\mathbf{a}}$ starting near the interface. While longer sampling may seem desirable, care must be taken to avoid sampling near the PMLs where the fields are rapidly attenuated and simulations with significantly larger computational domains becomes extremely challenging. Calculations with ordinary SPPs have verified that the attenuation behavior in the first few μm of propagation is generally representative of the SPP attenuation behavior. The figures and captions show that the FDTD results are reasonably well described by exponentials and that the resulting propagation lengths are in good accord with the Snell's law predictions.

3 Measurement of Leakage Radiation

Here we describe a simple experimental approach for measuring the leakage radiation of ISPPs. As described in the text, the leakage radiation angle of an SPP is related to its dispersion, and

so the unique dispersions predicted for ISPPs will have signatures in the leakage radiation. The experimental setup to leakage radiation involves an oil immersion microscope objective positioned below the glass substrate and sample, which can be used both to excite ordinary SPPs and collection of the resulting reflected light and SPP and ISPP leakage radiation. We illustrate this setup in Fig. S5.

The objective is capable of focusing a collimated light source to a spot containing incident wavevector rays with a range of values of χ_1 and θ_1. In principle, all values of θ_1 between 0 and 2π are possible, while χ_1 is limited by the numerical aperture (NA) of the objective to $\pm\sin^{-1}(\mathrm{NA}/1.5)$. This range of χ_1 will typically be sufficient to excite SPPs on silver and gold. In the following, we consider only ordinary SPPs excited on silver and their refraction at the silver-gold interface to generate gold ISPPs; λ_0 can be chosen, for example, such that no significant excitation of gold SPPs can occur. For simplicity, we assume an unpolarized light source so that there will always be a component of each ray that is consistent with p-polarization required for SPP generation. For a fixed λ_0, as discussed in the previous paragraph, only rays with $\chi = \chi_{KR}$ will couple into silver SPPs. However, because θ_1 can vary from 0 to 2π, SPPs will be launched with all possible angles of incidence with respect to the gold interface. The silver SPPs with θ_1 in the range $\{-\pi/2, \pi/2\}$ will refract at the gold interface to create ISPPs on the gold surface. The leakage radiation from the silver SPPs and the gold ISPPs will be collected by the objective, leading to the construction of a 2-D image. The image of the silver SPP leakage radiation will form a circular pattern with a radius proportionate to $\eta_1 \sin(\chi_1)$, with each point along the circle corresponding to a different in-plane propagation angle, θ_1. The ISPPs generated on gold by the silver SPPs will also contribute to the 2-D image of the collected radiation, but only in the region between $\{-\pi/2, \pi/2\}$ because they require excitation from silver SPPs propagating towards the silver/gold interface. Therefore, their leakage radiation will lead to a distorted semi-circular pattern with radii proportionate to $N_2 \sin(\theta_2)$, where both N_2 and θ_2 now depend on θ_1 according to the CSL.

We should note that for the explicit set-up of Fig. S5, with the excitation source below the metal film, there will also be a significant amount of *reflected* light collected by the 2-D detector. In fact, there will be a trough or minimum structure in the collected light signal around the ordinary silver SPP circle due to this reflection being minimized upon silver SPP excitation. The ISPP leakage radiation curve will actually add to the reflected light in this region and lead to a ridge or maximum structure on top of the background reflection. This latter structure can be further identified by comparison with the corresponding result for just a silver film in the absence of ISPPs. A background-free measurement of the leakage radiation is feasible if SPPs are excited from the superstrate side, which can be accomplished, for example, with an NSOM probe[2]. A set of dipole scatterers could also serve as the excitation source. In fact, SPP excitation by the emission of fluorescent molecules, and the subsequent collection of the SPP leakage radiation, forms the basis of the well-known surface plasmon coupled emission (SPCE) technique of Lakowicz and co-workers for silver and gold surfaces[3,4]. Based on the arguments presented in this text, we would expect SPCE to lead to characteristic leakage patterns that would reflect dispersion imprinting. While these measurements are straightforward in principle, we emphasize that the fabrication of a surface with a high-quality metal-metal interface is the final key ingredient for experimentally realizing our theoretical results. If the metal domains in a sample have an overlapping region, the SPP dispersion in this region will be different than the dispersion on either side of the interface, which will complicate matters in terms of controlling the ISPP properties. On the other hand, if a gap region exists between the two metals, this will cause scattering of the incident SPP, which will couple energy to the far field rather than into ISPPs. Consequently, we are currently developing

fabrication strategies to generate samples with high-quality metal-metal interfaces to enable the measurements described above.

4 Dependence of refraction angles and effective indices on incident angle

The angles of refraction (θ_2 and ϕ_2), as well as the effective ISPP index ($N_2 + iK_2$), depend on the incident angle (θ_1) via the Snell's law of Eqs. (5) and (6). A further subtle point is that $\sin^{-1}\theta_1$ required for their evaluation is multivalued, and θ_2 and ϕ_2 each have two possible values: the principal value, which will be between 0 and $\pi/2$, and what we will call the *secondary value*, which will be between $\pi/2$ and π. The secondary value is related to the principal value simply by $\theta^{SV} = \pi - \theta^{PV}$, where the superscript PV (SV) denotes the principal (secondary) value. Importantly, not all possible values of θ_2 and ϕ_2 satisfy the condition $N_2K_2\cos(\theta_2 - \phi_2) = \eta_2\kappa_2$ (Eq. (9) in the text). To resolve the apparent ambiguity in assignment of the angles of refraction, we note that for normal incidence ($\theta_1 = 0$), both θ_2 and ϕ_2 must be zero, so $\theta_2^{PV} = 0$ and $\phi_2^{PV} = 0$ is the only possible angle pair. For incident angles larger than 0, we assign the angles by choosing the angle pair that ensures that (a) Eq. (9) is satisfied and (b) both θ_2 and ϕ_2 vary smoothly as a function of θ_1, starting from $\theta_1 = \theta_2 = \phi_2 = 0$. Furthermore, we find that this choice also ensures that the transmission amplitude, T, varies smoothly with incident angle, while the opposite choice can lead to discontinuities and negative values of T.

The trajectories of θ_2 and ϕ_2, along with N_2 and K_2, as a function of θ_1 for the Au/Ag and Au/Al refraction examples are shown in Fig. S3 and S4. (Note that if one expands the scales in Fig. S4 in the $\theta_1 = 40$-50° range, the corresponding functions are actually smoothly varying.)

Other phenomena based on refraction, such as focusing by a lens, have analogs with absorbing material and can be treated with Snell's law. Fig. S6 demonstrates this with an SPP excited on a Al surface with a high-refractive index superstrate (e.g. diamond, $\epsilon = 6$) incident up a silver cylindrical lens, also coated with a superstrate with $\epsilon = 6$. At this frequency, we arrive at medium refractive indices $\eta_1 = 2.69, \kappa_1 = 0.075, \eta_2 = 4.08$, and $\kappa_2 = 0.064$. The ratio of η_1 to κ_1 is 0.66, analogous to geometric optics refraction at an air/glass interface. Hence, for small incident angles we expect similar focusing behavior as a glass lens in air, which is qualitatively seen in Fig. S6.

5 Finite-difference time-domain calculations

The Snell's law predictions were validated by numerical solution of Maxwell's equations using 3-D finite-difference time-domain (FDTD) calculations[5,6]. The structures described in the paper (see Fig. 1(a) of the main text) are represented on a uniform rectangular grid with spacings dx = dy = dz = 5 nm. A line of point dipoles situated just above metal 1 in its dielectric region is used to excite the incident SPPs. The actual calculations, employing our own 3-D FDTD code, were most conveniently accomplished by rotating the structure, as opposed to the source, in order to achieve various angles of incidence, a particular example being indicated in Fig. S7. The calculated results are then rotated to be consistent with the coordinate system in Fig. 1 of the main text. The overall size of the computational domain for a typical calculation is (x,y,z) = ($8\mu m$, 14μm, 0.725μm). We crop the field maps to highlight the behavior of the ISPPs over the normal propagation of the incident SPP. Fig. S7 represents a field map without rotation or cropping. The metal slabs

in all simulations have a thickness of 500 nm (in the z-direction) with a 40 nm dielectric layer above and 35 nm layer below the metal; a 75 nm thick pml is used above and below the dielectric layers. The metal permittivities are modeled using a Drude + two Lorentz form[6], with coefficients specifically fit for each example to closely reproduce the experimental permittivity values cited in the main text. The SPP excitation source is modeled by a line of point dipoles, positioned 10 nm above the surface of metal 1 (z = 620 nm), and spanning the width of metal 1 (approximately 8μm), each dipole oscillating at the desired excitation frequency. Perfectly matched layers[5] are used at the boundaries of the computational domain. The FDTD simulation evolves the electric (and magnetic) fields with a time-step of approximately 1.8 x 10^{-17} s for a total time of 100 fs; for the computational domains considered, such a simulation typically takes about one hour on 120 processors.

To image the surface wave propagation, the z component of the FDTD electric field, $E_z(t)$, is Fourier transformed on the excitation frequency ω to obtain the frequency domain result, $E_z(\omega)$. (Other components yield similar results.) This represents the complex phasor field at this frequency that is associated with an actual, real electric field time-dependence given by $E_z(t) = \mathrm{Re}\left[E_z(\omega)\exp(-i\omega t)\right]$. An instantaneous field or a snapshot, which contains phase information, is obtained by evaluating this latter expression for some arbitrary value of t which we take to be $t = 0$. The associated field intensity is the time average of the square of the instantaneous field, which is of course $|\mathbf{E}_z|^2$. For simplicity, the spatial dependence has been suppressed in the above discussion. Generally, the fields are evaluated for in a plane of x,y values at a z value corresponding to about 120nm above the metal surfaces.

1. Chang, P. C. Y.; Walker, J. G.; Hopcraft, K. I. Ray tracing in absorbing media. *J. Quant. Spectrosc. Radiat. Transfer* **2005**, *96*, 327-341.

2. Hecht, B.; Bielefeldt, H.; Novotny, L.; Inouye, Y.; Pohl, D. W. Local excitation, scattering, and interference of surface plasmons. *Phys. Rev. Lett.* **1996**, *77*, 1889-1893.

3. Lakowicz, J. R.; Malicka, J.; Gryczynski, I.; Gryczynski, Z. Directional surface plasmon-coupled emission: a new method for high sensitivity detection. *Biochem. Biophys. Res. Commun.* **2003**, *307*, 435-439.

4. Gryczynski, I.; Malicka, J.; Gryczynski, Z.; Lakowicz, J. R. Surface Plasmon-Coupled Emission with Gold Films. *J. Phys. Chem. B* **2004**, *108*, 1256812574.

5. Taflove, A; Hagness, S. C. *Computational Electrodynamics: the finite-difference time-domain method* 2$^{\mathrm{nd}}$ ed. (Artech, 2000).

6. Montgomery, J. M.; Lee, T.-W.; Gray, S. K. Theory and modeling of light interactions with metallic nanostructures. *J. Phys.: Conds. Mater* **2008**, *20* 323201-323222.

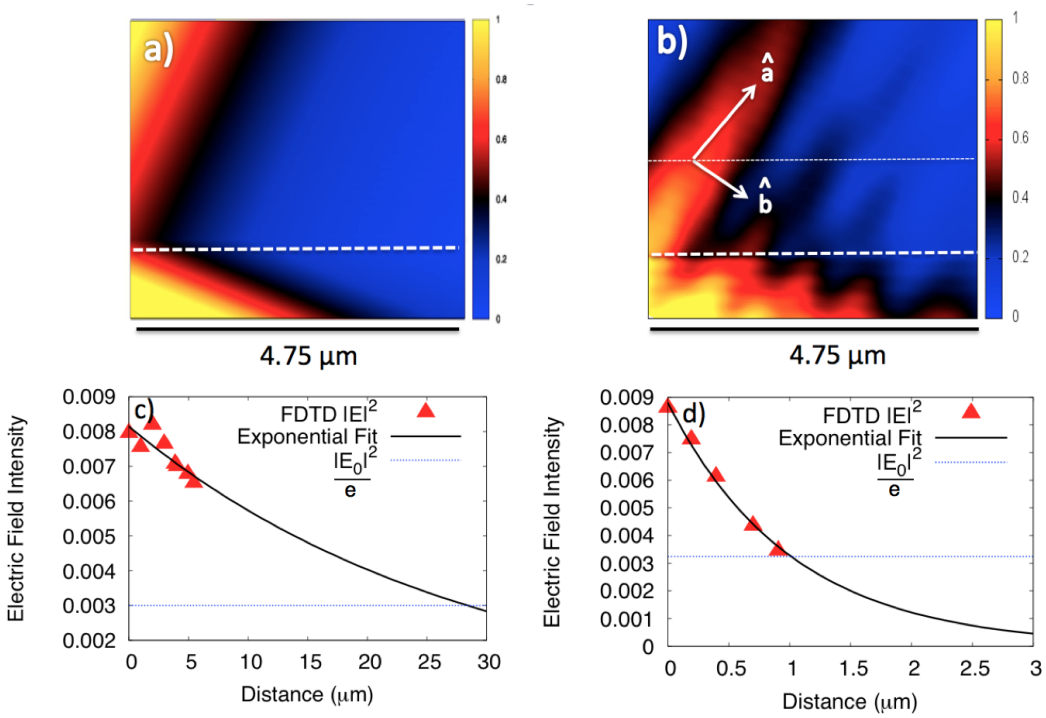

Figure S1: (a) and (b) : Electric field intensities, $|\mathbf{E}|^2$, for an SPP on Au (below dashed white line), being refracted onto Ag (above white dashed line). The angle of incidence is 25°, the vacuum wavelength is 532 nm, and air is assumed to be above both metals. The Snell's law result is in panel (a) and the rigorous electrodynamics calculation, via the FDTD method, is in panel (b). (c) The propagation length is calculated by evaluating $|\mathbf{E}|^2$ from the electrodynamics calculation along the vector $\hat{\mathbf{a}}$ and fitting an exponential function. Snell's law predicts that the vector $\hat{\mathbf{a}}$ will point approximately 27° from the normal to the interface at the white dashed line. The exponential, solid curve, crosses $|\mathbf{E}_0|^2/e$ at 28 μm, in excellent agreement analytical prediction of 27 μm from the Snell's law. (d) The confinement length is calculated by evaluating $|\mathbf{E}|^2$ from the electrodynamics calculation along the vector $\hat{\mathbf{b}}$ and fitting an exponential function to the field values. Snell's law predicts that the vector $\hat{\mathbf{a}}$ will point approximately 114° to the normal to the interface. The exponential, solid curve, crosses $|\mathbf{E}_0|^2/e$ at 1.1 μm, also in good agreement analytical prediction of 1.7 μm from Snell's law.

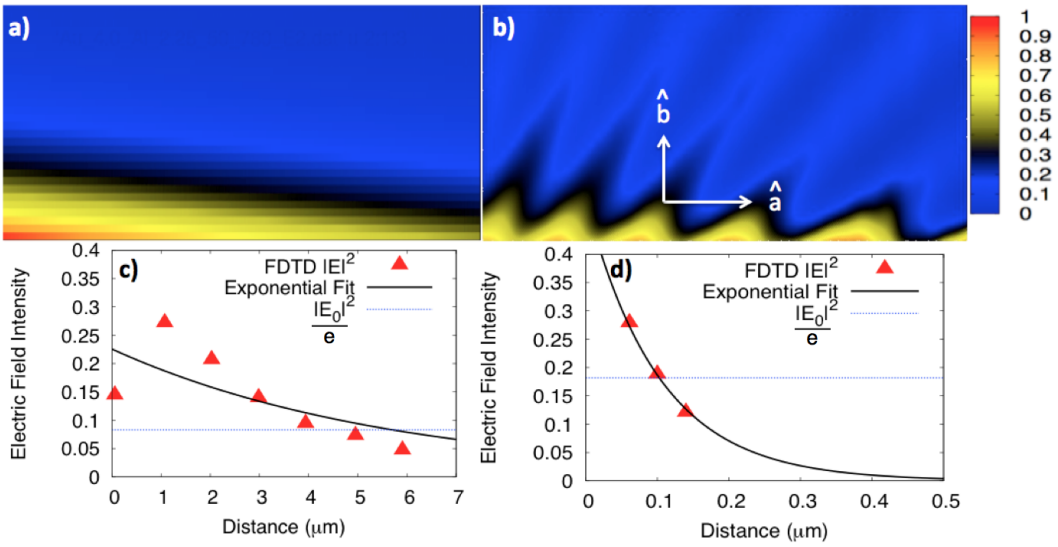

Figure S2: Snapshot of Re(E_z), ((a) and (b)), and electric field intensities, $|\mathbf{E}|^2$ ((c) and (d)) resulting from an SPP on Au being refracted onto Al. The angle of incidence is 50°, the vacuum wavelength is 780 nm. An $\epsilon_1^D = 4$ dielectric is assumed to be above the Au surface, and glass ($\epsilon_2^D = 2.25$) is assumed to be above the Al surface. Only the refracted (on Al) portion is displayed. Snell's law results are plotted in (a) and (c) and results from FDTD calculation are plotted in (b) and (d). The propagation length is calculated by evaluating field intensity from the electrodynamics calculation along the vector $\hat{\mathbf{a}}$ and fitting an exponential function. Snell's law predicts that the vector $\hat{\mathbf{a}}$ will point approximately 90° from the normal to the interface. The exponential, plotted in (e), crosses $|\mathbf{E}_0|^2/e$ at 5.6 μm, in excellent agreement analytical prediction of 5.6 μm from Snell's law. The confinement length is calculated by evaluating $|\mathbf{E}|^2$ from the electrodynamics calculation along the vector $\hat{\mathbf{b}}$ and fitting an exponential function to the field values. Snell's law predicts that the vector $\hat{\mathbf{a}}$ will point approximately 1° to the normal to the interface. The exponential, plotted in (f), crosses $|\mathbf{E}_0|^2/e$ at 0.1 μm, also in agreement analytical prediction of 0.08 μm from Snell's law.

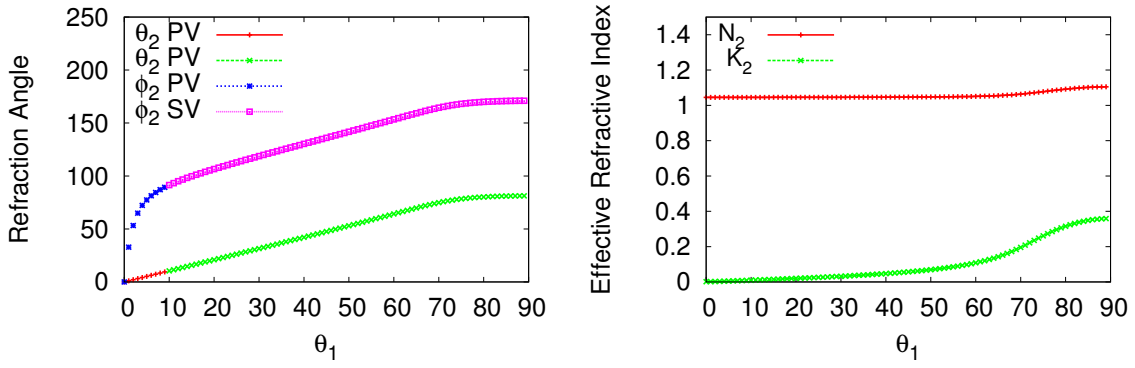

Figure S3: (Left) Trajectory of refraction angles θ_2 and ϕ_2 as a function of θ_1 for an SPP excited by 532 nm light on a gold surface with air above (medium 1) and refracting onto an aluminum surface with glass above (medium 2). For incident angles larger than 9°, the principal values of θ_2 and ϕ_2 do not satisfy Eq. (9). The angle pair $(\theta_2^{PV}, \phi_2^{SV})$ maintains continuity beyond $\theta_1 = 9°$. (Right) Trajectory of effective refractive indices for the ISPP as a function of θ_1.

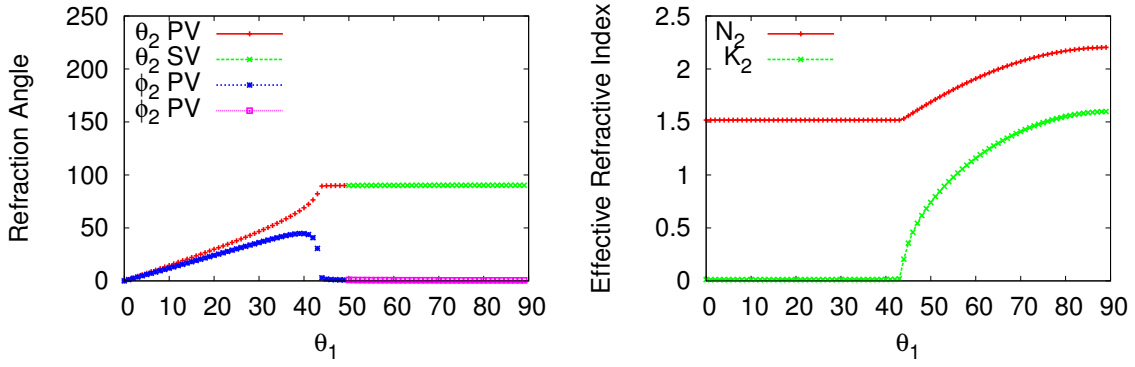

Figure S4: (Left) Trajectory of refraction angles θ_2 and ϕ_2 as a function of θ_1 for an SPP excited by 780 nm light on a gold surface with $\epsilon = 4$ above (medium 1) and refracting onto an aluminum surface with glass above (medium 2). For incident angles larger than 50°, the principal values of θ_2 and ϕ_2 do not satisfy Eq. (9). The angle pair $(\theta_2^{SV}, \phi_2^{PV})$ maintains continuity beyond $\theta_1 = 50°$. (Right) Trajectory of effective refractive indices for the ISPP as a function of θ_1. Dramatic departure of both effective indices from the material indices can be seen starting at $\theta_1 = 45°$. This strong departure can also be seen in the imprinted dispersion in Fig. 3 in the main text.

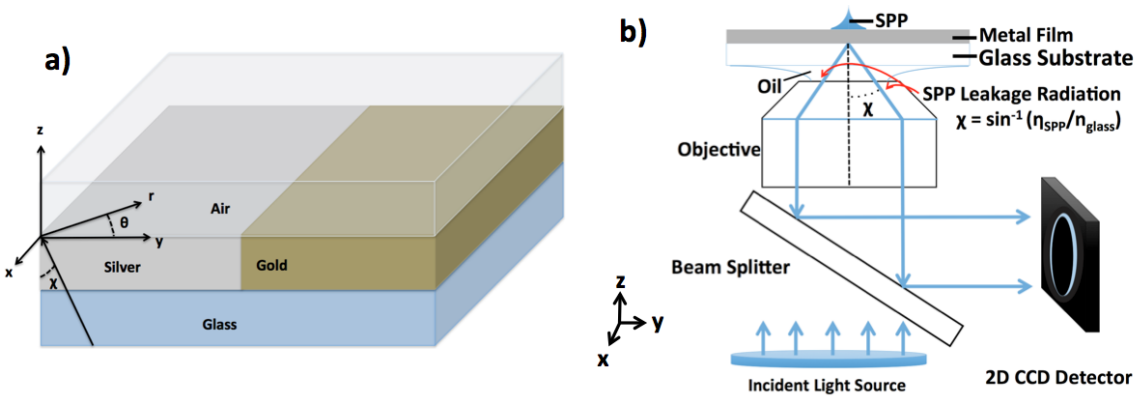

Figure S5: **a)** Schematic of interfaced metal film samples where ordinary SPPs can be excited from the glass side by varying the angle χ to match the incident wavevector with the SPP wavevector. The angle of incidence with respect to the interface between gold and silver is given by the angle θ. The films must be relatively thin (less than 100 nm) both to allow excitation of SPPs from the glass side and for there to be measurable leakage radiation. **b)** Schematic of microscope objective which can be used to collect leakage radiation. The same setup can be coupled with a light source for excitation of SPPs, as described in the text.

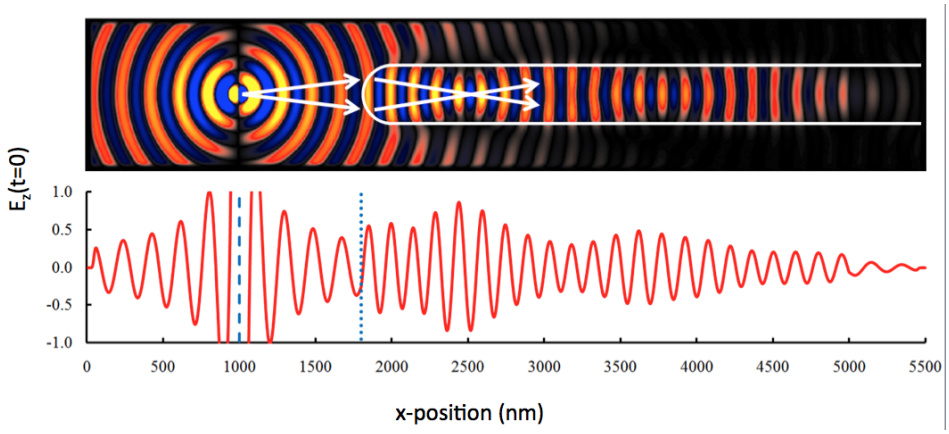

Figure S6: FDTD calculations of an SPP excited by 495 nm light on an Al surface, and focused by a cylindrical Ag lens region. A $\epsilon = 6$ dielectric material is assumed to be above both regions. Upper image: snapshot of Re(E_z) 10 nm above the film surface. The Ag film is outlined in white. Lower image: slice through the middle of the upper image. The blue dashed line indicated the dipole position, and the blue dotted line indicates the surface of the Ag film.

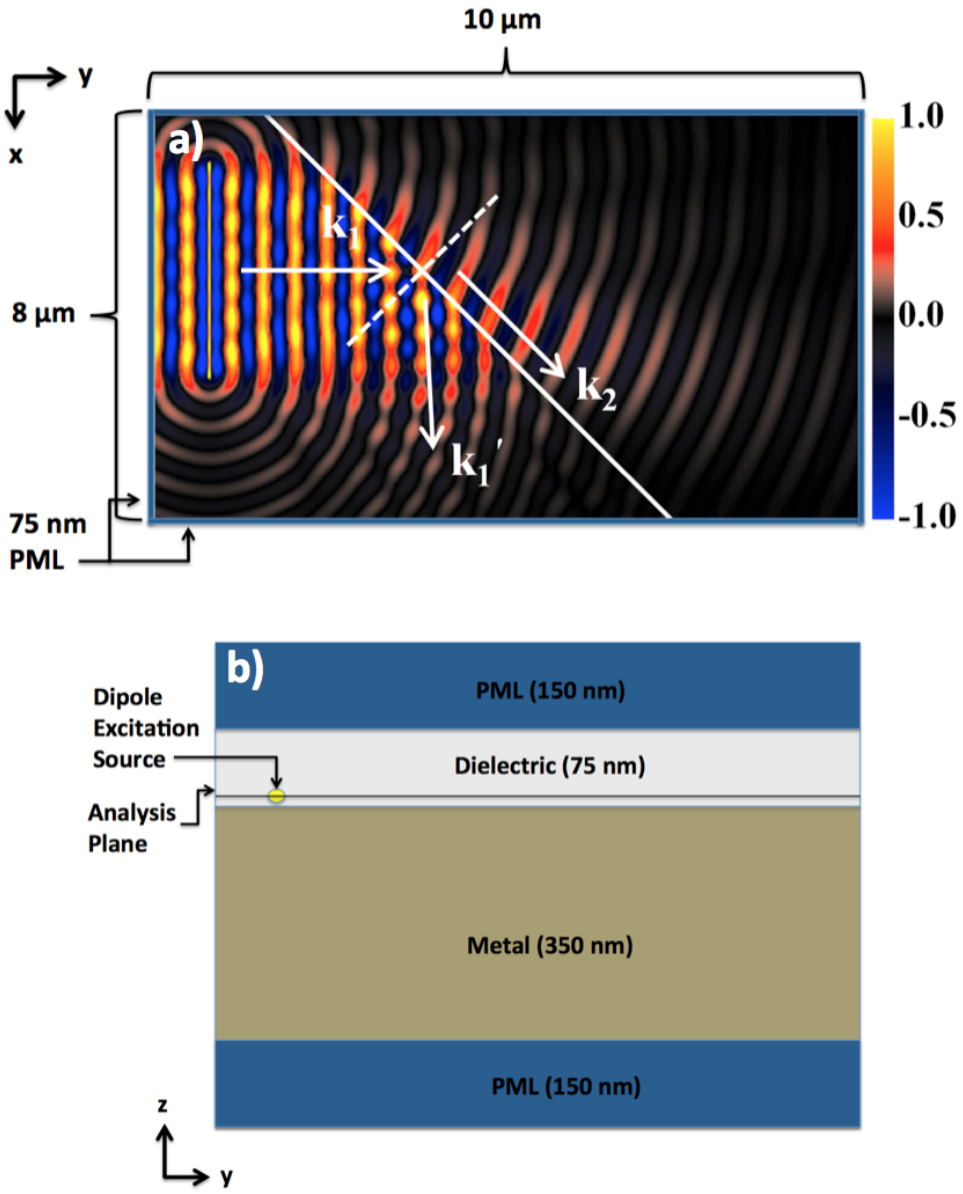

Figure S7: Illustrative figure showing FDTD calculation of SPP refraction. (a) is a 2-D cut of the instantaneous field, Re(E_z), in the x-y plane at a z value corresponding to 10 nm above the metal surfaces. The excitation source (an $\approx$ 5 μm line of point dipoles also 10 nm above the metal surface) is evident on the left, and generates an SPP with wavevector $\mathbf{k_1}$ incident upon an angled interface between medium 1 and medium 2 (solid white line). The computational domain is typical of the calculations presented in the main text - spanning 8μm in x, 10μm in y, and 0.725μm in z. The SPP is reflected ($\mathbf{k_1'}$) and refracted ($\mathbf{k_2}$) at the interface. The actual example shown corresponds to medium 1 being Ag, medium 2 being Al, $\epsilon = 6$ dielectric above each metal, and 496 nm incident light, which yields a TIR-like ISPP wave in medium 2. The the outer 75 nm of the domain consists of perfectly matched layers (PML). (b) is a schematic representation of an y-z slice of the computational domain, showing the 350 nm metal slab with 75 nm dielectric layer above as well as 150 nm PMLs on top and bottom. The approximate z-positon of the line of dipoles and the analysis plane (where the fields are imaged) is also indicated.